

Research Article

<https://doi.org/10.1631/jzus.A2400396>

An energy-saving design method for additively manufactured integrated valve-controlled cylinders

Yang TANG^{1*}, Dengting LI^{1*}, Honghao LIU¹, Chao ZHANG¹, Wujun WANG², Jie Cai³, Huayong YANG¹, Yi ZHU^{1,4}✉

¹State Key Laboratory of Fluid Power and Mechatronic Systems, Zhejiang University, Hangzhou 310058, China

²Department of Energy Technology, KTH Royal Institute of Technology, Stockholm 10044, Sweden

³China Railway Construction Heavy Industry Corporation Limited, Changsha 410023, China

⁴Ningbo Innovation Center, Zhejiang University, Ningbo 315100, China

Abstract: The integrated valve-controlled cylinder combines various control and execution components in hydraulic transmission systems. Its precise control and rapid response characteristics make it widely used in mobile equipment for aerospace, robotics, and other engineering applications. Additive manufacturing provides high design freedom which can further enhance the power density of integrated valve-controlled cylinders. However, there is a lack of effective design methods to guide the additive manufacturing of valve-controlled cylinders for more efficient hydraulic energy transmission. This study accordingly introduces an energy-saving design method based on additive manufacturing for integrated valve-controlled cylinders. The method consists of two main parts: (1) redesigning the manifold block to eliminate leakage points and reduce energy losses through integrated design of the valve, cylinder, and piping; and (2) establishing a pressure loss model to achieve energy savings through optimized flow channel design for bends with different parameters. Compared to traditional valve-controlled cylinders, the integrated valve-controlled cylinder developed from our method reduces the weight by 31%, volume by 55%, and pressure loss in the main flow channel by over 30%. This indicates that the design achieves both lightweight construction and improved hydraulic transmission efficiency. This study provides theoretical guidance for the design of lightweight and energy-efficient valve-controlled cylinders, and may aid the design of similar hydraulic machinery.

Key words: Valve-controlled cylinder; Additive manufacturing; Flow channel design; Energy saving machinery; Integration

1 Introduction

The valve-controlled cylinder is a crucial power unit within hydraulic transmission systems, and is typically comprised of a motor, pump, controller, various control valves, and a hydraulic cylinder (Padovani et al., 2020). It enables local and independent movement, and finds application in aerospace, robotics, and other engineering machinery (Wu et al., 2020; Zhang et al., 2018; Abinab et al., 2018). Metal additive manufacturing technology currently holds

significant potential for development in molding manufacturing methods (Huang et al., 2015; Kumar et al., 2021). This approach operates on the principle of piecewise superposition to create three-dimensional objects with significant design flexibility (Prakas et al., 2018), offering new possibilities for enhancing the performance, integration, and lightweight nature of valve-controlled cylinders.

For integrated valve-controlled cylinders with multiple components, additive manufacturing technology simplifies the original component layout. It reduces the number of connection joints and auxiliary process holes, and significantly decreases the weight of valve-controlled cylinders (Xie et al., 2020; Langelaar et al., 2018). It also eliminates sharp bends, resulting in improved flow channels (Stephen et al., 2021; Zhang et al., 2020; Pietropaoli et al., 2017). Moog collaborated with an Italian research institute to develop an integrated valve-controlled cylinder that

✉ Yi ZHU, yiz@zju.edu.cn

* The two authors contributed equally to this work

Received Aug. 19, 2024; Revision accepted Dec. 3, 2024;
Crosschecked

utilized additive manufacturing to integrate hydraulic cylinders, servo valves, sensors, and connecting channels. The cylinder achieved high-performance control while reducing energy loss and compacting the entire actuator structure (Victor et al., 2018). Wang et al. (2021) redesigned a three-degree-of-freedom robot actuator with a rotating hydraulic cylinder using additive manufacturing technology, which increased the output torque of the actuator while reducing its weight and volume. Boston Dynamics used additive manufacturing to form an entire leg actuator, improving the hydraulic flow channel efficiency and enhancing the cooling capacity, and utilized multi-materials for increased functionality and durability of the part (Bhatti et al., 2015; Siavash et al., 2018). Huang et al. (2021) employed additive manufacturing technology to develop lightweight designs for actuators, specifically utilizing topology optimization and carbon fiber composites to eliminate excess materials and reduce the overall weight of an actuator by more than 50%. In terms of flow channel optimization, Coletti et al. (2013) utilized segmented Bessel parameter curves to optimize U-shaped pipes fabricated through additive manufacturing, and achieved a 36% reduction in pressure loss. Similarly, Zhang et al. (2019) introduced a flow channel generation and connectivity rule, employing a layout method to construct three-dimensional flow channel models. This approach resulted in a 74.6% decrease in pressure loss for typical internal flow channels and a 25.1% reduction in total volume. The actuator design discussed above has served as an important reference for designing integrated valve-controlled cylinders. However, current research primarily focuses on designing component structures based on existing experience, without establishing scientific design criteria or processes for additive manufacturing of the cylinders.

Therefore, this study presents a design method for energy-saving integrated valve-controlled cylinders using additive manufacturing. Following the redesign and remanufacturing of a traditionally processed valve-controlled cylinder, the performance of the resulting cylinder is tested, with the goal of achieving lower weight and energy savings.

2 Prototype of the traditional valve-controlled cylinder

Fig. 1(a) depicts a conventional machined valve-controlled cylinder structure, featuring an electromagnetic directional valve, a hydraulic mani-

fold block, and a combination of hydraulic cylinders. Its functionality relies on the integrated superposition of various functional components. These components operate independently, and the mechanical connections introduce numerous interfaces, thereby increasing the risk of leakage. Fig. 1(b) illustrates the hydraulic schematics of the valve-controlled cylinder system. Fluid is pumped from the tank by a motor-driven pump, passes through a filter and throttle valve, and is then controlled by an electromagnetic directional valve. This setup regulates the inflow and outflow of hydraulic oil to achieve piston rod expansion and contraction within the cylinder. The relief valve vents high pressure. The material used for this valve control cylinder is 316L stainless steel; it weighs 10.37 kg with dimensions of $310 \times 97 \times 185 \text{ mm}^3$.

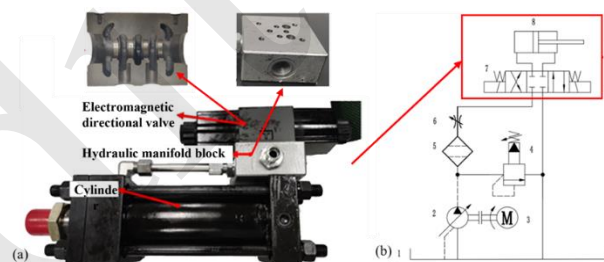


Fig. 1 (a) Conventional machined valve-controlled cylinder; (b) Schematics of the hydraulic transmission system

3 Integrated structural design

Traditional valve-controlled cylinder structures rely on a stacked assembly of components, which can lead to a significant increase in system weight and volume, as well as a reduction in power density (Shang et al., 2018; Quan et al., 2014). Additive manufacturing enables the integration of multiple functional components into the hydraulic cylinder surface, facilitating energy savings and lightweight design through anisotropic structures that are challenging to construct using traditional processing methods. The overall structural design encompasses flow channel logic and integrated design of functional interfaces.

Fig. 2(a) illustrates the individual working oil holes in the original electromagnetic directional valve, while Fig. 2(b) depicts the individual working oil holes in the integrated valve-controlled cylinder. When designing for integration, it is essential to ensure that one-to-one correspondence is maintained

and the functionality unchanged after integration. Once the original functional interfaces are replicated, they should be connected based on their connection logic.

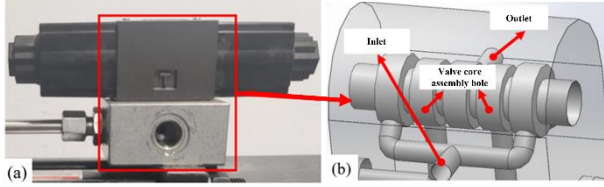


Fig. 2 (a) Integration of the traditional prototype valve body and manifold block; (b) Integrated valve body and manifold block integration

Utilizing the freedom of design offered by additive manufacturing, each interface is rearranged while ensuring the integrity of the original flow channel logic. In the layout design, Eq. (1) denotes the total number of assembly holes in the valve-controlled cylinder, and Eq. (2) represents the cumulative length of the flow channel:

$$N_{\min} = n_1 + n_2 + \dots + n_j \quad (1)$$

$$L_{\min} = l_1 + l_2 + \dots + l_i \quad (2)$$

Here, N_{\min} is the minimum total number of assembly holes of the valve-controlled cylinder; n_j is the number of assembly holes in the valve-controlled cylinder; L_{\min} is the cumulative length of the valve-controlled cylinder flow channel; l is the length of each section of the flow channel; i is the total number of flow channels in the valve-controlled cylinder.

In this integrated design, our primary objective is to minimize the number of assembly holes and integrate each assembly interface directly with the flow channel or with other functional components. Simultaneously, we want to optimize the design for the shortest flow channel length and segment count. For instance, the design reduces local channels in the manifold block by directly integrating inlet and outlet holes, while a wall-mounted design is used to distribute flow channels both inside the manifold block and on the surface of the cylinder.

Table 1 illustrates the reduced height and weight of the valve-controlled cylinder, as well as the increased level of integration resulting from the use of an integrated design. This approach also minimizes the number of assembly holes for the

valve-controlled cylinder, thereby reducing post-production machining requirements, streamlining assembly processes, enhancing system reliability, and mitigating the risk of hydraulic fluid leakage.

Table 1 Comparison between traditional manifold block integration and integrated manifold block integration

Parameters	Traditional assembly integration	Integrated integration
Height (mm)	120	70
Weight (kg)	1.94	1.16
Number of electromagnetic directional valve assembly holes	10	2
Number of connecting flow channel assembly holes	14	2

4 Integrated design of shared walls

When the flow channel is close to the cylinder surface in the integrated design, this shortens the length and reduces the volume of the valve-controlled cylinder. This also minimizes the support requirements during formation and subsequent machining processes. However, the use of shared walls can result in stress concentrations that cause reduced strength. In this study, ANSYS software was used to conduct stress modeling of the cylinder. A working pressure of 21 MPa was applied to both the valve-controlled cylinder and the internal flow channel. Displacement constraints were also imposed perpendicular to the unsealed end face to restrict movement in that direction. Fig. 3 depicts the stress distribution in the shared wall between a flow channel and a cylinder, with both having a 6 mm inner diameter. Compared to a single flow channel, there is an increase in maximum von Mises equivalent stress, particularly near the wall shared with the 6 mm flow channel.

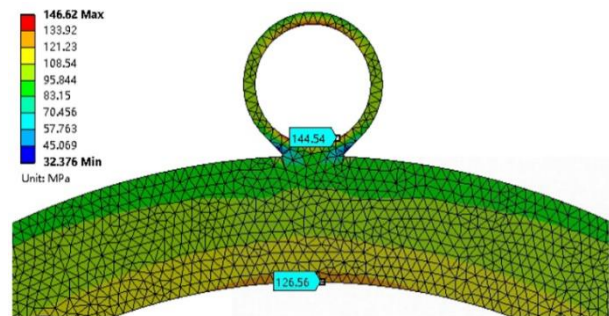


Fig. 3 Stress distribution in a shared wall

Both the flow channel and the inner side of the cylinder are subjected to a uniform load of oil pressure. Upon application of oil pressure, radial stresses and circumferential stresses are induced within the flow channel, causing both the flow channel and the cylinder to have a tendency to expand outward. However, at the junction between the flow channel and the cylinder, deformation in the radial direction is constrained, leading to increased deformation in the circumferential direction and a significant rise in circumferential stress at this location. Consequently, the point connecting the centers of the flow channel and the cylinder is where deformation is most restricted, resulting in the generation of maximum circumferential stresses. The integration between the flow channel and cylinder block connection leads to higher maximum stresses in the channels compared to those for a single channel.

By increasing the flow channel wall thickness and adjusting the diameter ratio of large-to-small flow channels, it is possible to reduce the stresses on the channels without altering the channel structure. Fig. 4 illustrates the maximum equivalent stresses of the channel and cylinder at various diameter ratios, showing that stress levels effectively decrease as the diameter ratio increases.

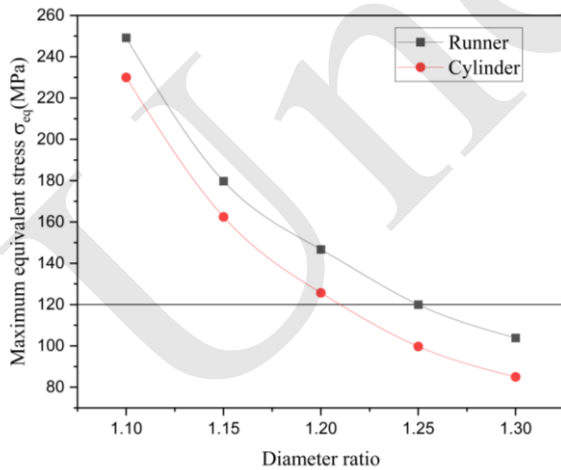


Fig. 4 Maximum equivalent stress of the flow channel and cylinder at various diameter ratios

Thus, when determining the distance for pressure-bearing components such as flow channels, it is essential to establish an appropriate distance that allows the component to deform freely under forces

while not altering its original shape. For this type of pressure vessel channel, the stress magnitude is only considered under internal pressure conditions, as depicted in Eqs. (3), (4), and (5):

$$\sigma_{\theta} = \frac{P}{(k^2 - 1)} \left(1 + \frac{R_o^2}{r^2}\right) \quad (3)$$

$$\sigma_r = \frac{P}{(k^2 - 1)} \left(1 - \frac{R_o^2}{r^2}\right) \quad (4)$$

$$\sigma_z = \frac{P}{k^2 - 1} \quad (5)$$

Here, σ_{θ} , σ_r , and σ_z respectively represent the circumferential stress, radial stress, and axial stress borne by the flow channel; k is the ratio of the outer diameter to the inner diameter of the flow channel; P is the internal pressure borne by the flow channel; R_o is the outer diameter of the flow channel; r is the distance from a point in the channel wall to the center of the channel circle.

According to Hooke's law, the deformation condition of the circumferential flow channel under triaxial stress is:

$$e_t = \frac{1}{E} (\sigma_t - \mu\sigma_r - \mu\sigma_z) \quad (6)$$

According to the deformation of the outer wall of the flow channel, we can obtain:

$$e_t = \frac{\Delta R}{R_o} \quad (7)$$

Thus, the radial deformation of the flow channel is:

$$\Delta R = \frac{(2 - \mu)PR_o}{E(k^2 - 1)} \quad (8)$$

When using additive manufacturing technology to form channels, the influence of the laser spot diameter r can result in the formed entity being larger than the intended design size (Jordan et al., 2022; Michael et al., 2017). Therefore, when designing channel spacing, it is necessary to consider the impact

of the laser spot diameter. Assuming that the deformations in the radial direction of two neighboring parallel channels are ΔR_1 and R_2 , and that θ is the angle between a line connecting their centers and the horizontal line, then the designed gap for the horizontally formed channels is:

$$d = \Delta R_1 + \Delta R_2 + r / \cos \theta \quad (9)$$

The above formula is applicable for channels that share the same starting plane and are parallel to each other. When dealing with channels with overlapping angles or structures, printing parameters and the influence of support on channel formation must be considered in the spacing design.

5 Method for planning low-pressure loss channel paths

In valve-controlled cylinders, conventional flow channels are primarily shaped through drilling, milling, and other machining methods to achieve a change of direction with intersections mainly at right angles (Xu et al., 2019; Daniel et al., 2019). This type of transition not only leads to significant local pressure loss but also limits channel design. Additive manufacturing offers a high degree of design freedom, enabling new concepts for hydraulic unit channel design. The pressure loss in hydraulic channels typically consists of frictional pressure loss and local pressure loss. While there is an accurate model for calculating the frictional pressure loss in additive manufacturing flow channels (Zhou et al., 2021), there is a lack of models that can precisely predict local pressure loss.

5.1 Bent channel pressure loss model

In this study, computational fluid dynamics (CFD) is employed to conduct simulations of channels with varying bending ratios and angles under specific inlet conditions. The aim is to reveal the relationship between bending ratio, bending angle, and channel pressure loss in order to predict pressure loss in channels. Fig. 5 illustrates the simulated channel model. To ensure fully developed flow before the curved channel and to mimic realistic laminar flow conditions, a long straight flow channel precedes the bent flow channel, with measurement points

placed at specific distances.

The pressure loss at a bend is primarily attributed to two factors: frictional losses and losses caused by fluid separation during the turning process (Crawford et al., 2007). When the curvature ratio of the channel—defined as the ratio of the channel bend radius to the channel radius—is small, the pressure loss in the curved section is predominantly due to fluid separation. On the contrary, when the curvature ratio is relatively large, frictional losses become the main contributor to pressure loss.

For channels with high curvature ratios under consistent inlet and boundary conditions, the pressure loss can be estimated using (Hashan et al., 2021):

$$P = pR\theta \quad (10)$$

Here, R is the bending ratio of the flow channel (the ratio of the turning radius of the bend to the radius of the flow channel); θ is the bending angle of the flow channel; p is the pressure loss per unit length at a specific bending angle, under stabilized conditions where fluid friction predominantly governs the pressure loss.

For flow channels with low bending ratios, however, accurate estimation formulas remain elusive. To address this gap, we conducted simulations and interpolation techniques to evaluate the pressure loss in channels with specified bending ratios. As a result, a correlation was established among the bending ratio, bending angle, and flow channel pressure loss, providing a reliable method to predict pressure loss.

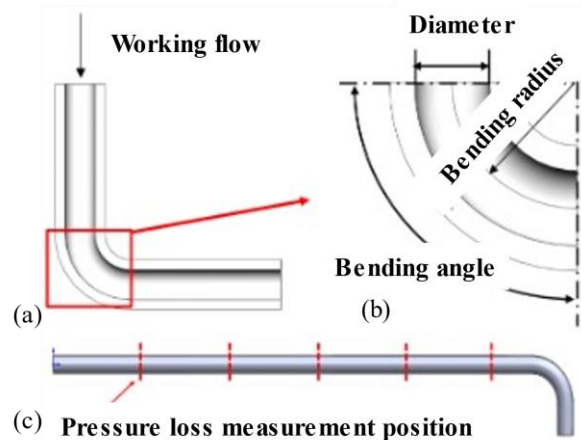


Fig. 5 Characteristic parameters of the bent channel

The working flow rates are set to 5 L/min, 15 L/min, 30 L/min, and 60 L/min, based on reference values for the valve-controlled cylinder. The simulation parameters are provided in Table 2. Based on the CFD simulation data points, the relationship is established using a bilinear interpolation function. Fig. 6 illustrates the pressure loss in the cornering flow channel for varying operating flow rates, bending angles, and bending ratios. It is evident that as the bending ratio increases, the pressure loss of the channel initially decreases before rising again. This occurs because fluid separation is the primary cause of pressure loss in the bent channel at lower bending ratios; as the bending ratio increases, the fluid separation diminishes. At the same time, the elongated path of the bent channel causes an increase in wall friction-induced pressure loss. Once it surpasses a certain threshold, wall friction becomes the primary cause of pressure loss in the channel and exhibits a strong linear correlation with the bending ratio.

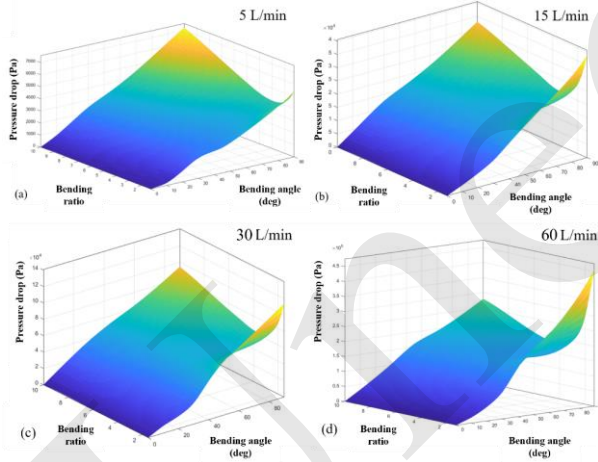


Fig. 6 Plots of bending angle, bending ratio, and pressure loss in the inflection channel for operating flow rates of (a) 5 L/min; (b) 15 L/min; (c) 30 L/min; and (d) 60 L/min, respectively

Table 2 Simulation calculation parameters

Parameters	Values
Feature length (mm)	6
Working medium	46#
Viscosity (Pa s)	0.03956
Density (kg/m ³)	860
Temperature (°C)	40
Grid shape	Hexahedral mesh
Speed inlet boundary conditions (m/s)	8.84, 17.68, 26.52, and 35.36

Pressure outlet boundary conditions (Pa)	0
Solving models	RNG k-ε
Residual convergence tolerance	10 ⁻⁶
Iterations	1500

5.2 Mathematical model for low-pressure loss channel path design

The theoretical prediction of pressure loss for a channel in any given condition can be obtained using the aforementioned database. For example, Fig. 7 illustrates the hydraulic component formed by additive manufacturing and its flow channels. The flow channels of the valve-controlled cylinder can be divided into DC channels l_1 , l_2 , and l_3 , as well as bent channels S_1 , S_2 , and S_3 .

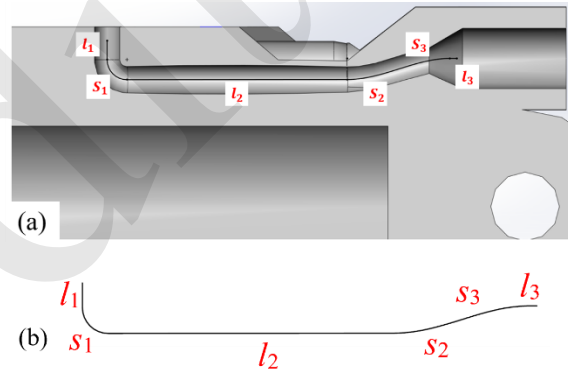


Fig. 7 (a) Additive manufacturing constructed valve-controlled cylinder; (b) Channel path in the cylinder

For an incompressible steady-flow fluid, the average velocity of the fluid remains constant when the inlet cross-sectional area is equal to the outlet cross-sectional area. In other words, it is necessary to calculate the average velocity at the inlet of each straight and curved channel to assess the operating flow rate for steady-state operation. Once the bending radius and bending angle of each corner channel are determined, pressure loss for that corner channel can be obtained by querying the database from a previous section. An evaluation function for assessing flow performance within a valve-controlled cylinder's flow channel is established as shown:

$$p_{\min}(Q) = \sum p_s(Q, R, \theta) + \sum p_l(Q) \quad (11)$$

Here, p_{min} is the minimum pressure loss value for the function; $\sum \Delta p_s(Q, R, \theta)$ is the sum of the pressure loss values of the bent channels at the working flow rate Q , bending ratio R , and bending angle θ ; $\sum \Delta p_1(Q)$ is the sum of all DC channels' pressure loss values at the working flow rate Q .

When designing hydraulic component channels, the known input condition typically involves the operating flow rate. Therefore, it is essential to establish the mathematical relationship between variations in channel shape, position, and other parameters of the corner and DC channels. This will enable us to predict the pressure loss across the channel. Fig. 8 illustrates the use of 3D coordinates for extracting parameters of the corner and DC channels, aiding the solution of the objective function:

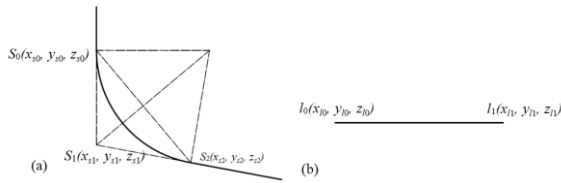


Fig. 8 (a) Bent channel parameters; (b) DC channel parameters

For the bent channel, the parameters used to estimate its pressure loss include the starting spatial coordinate S_0 , the bend point spatial coordinate S_1 , and the endpoint spatial coordinate S_2 . The bending angle θ is calculated using a vector composed of three points and can be obtained from Eq. (12):

$$\theta = \arccos\left(\frac{S_0 S_1 \cdot S_1 S_2}{|S_0 S_1| * |S_1 S_2|}\right) \quad (12)$$

And the bending ratio R can be calculated as:

$$R = \frac{R_s}{r} = \frac{S_0 S_2}{2 \times r \times \sin(\theta / 2)} \quad (13)$$

Here, R_s is the bending radius of the turning channel and R is the radius of the turning channel.

For the DC channel, knowing only the starting and ending coordinates is sufficient, and the length can be obtained using Eq. (14), and then used to estimate its pressure loss.

$$l = \sqrt{(x_{i1} - x_{i0})^2 + (y_{i1} - y_{i0})^2 + (z_{i1} - z_{i0})^2} \quad (14)$$

In designing the flow channel for the valve-controlled cylinder, it is essential to avoid interference with existing functional interfaces and necessary assembly space. Based on common component interface types and assembly space requirements for the valve-controlled cylinder, obstacles can be simplified into two categories: cylindrical (e.g., oil hole interfaces, cartridge valve interfaces, and their corresponding assembly spaces) and rectangular (e.g., plate valve assemblies).

5.3 Design of low-pressure loss flow channels for energy-saving valve-controlled cylinders

Including a bend in the channel of the cylinder helps to circumvent obstacles but also results in increased pressure loss. Therefore, optimizing the bend path design is crucial, as illustrated in Fig. 9.

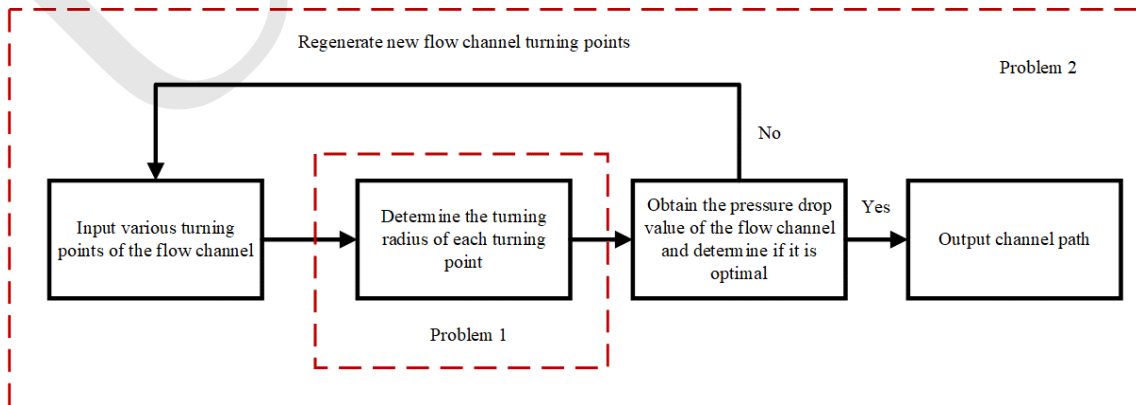


Fig. 9 Strategy for designing channels with minimal pressure loss

This solution process presents two primary challenges: (I) determining the optimal turning radius for each channel bend with predetermined locations; and (II) comparing channels at different locations and identifying relatively optimal channels within global constraints.

The objective is to determine the turning radius of each segment within the flow channel along a given path. These turning radius values may be interdependent, as illustrated in Fig. 10(a). For instance, the turning radius of channel S_1 can affect the range of possible values for the turning radius of channel S_2 . Alternatively, these radii can be independent, as shown in Fig. 10(b). Independence occurs when a "buffer channel" l_1 exists between turning channels S_1 and S_2 , allowing their radii to vary independently. Therefore, solving this problem requires addressing multivariable coupling. To determine whether the two curved channels are mutually constrained or independent, the length of l_1 must be evaluated.

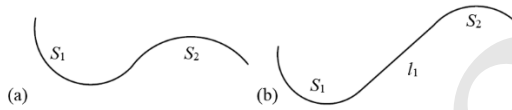


Fig. 10 (a) Two turning channels that are mutually constrained; (b) Independent turning channels

Given that the number of bends in a single flow channel within a valve-controlled cylinder is relatively small, the optimization variables for minimizing pressure loss are limited to the turning radii of these bends. This constraint leads to a relatively small computational workload. Consequently, solving Problem I could potentially involve enumerating across all possible configurations while ensuring that the iteration speed satisfies engineering requirements. Of course, the ultimate goal is to obtain the global optimal solution. Considering these factors, we selected the Simulated Annealing Algorithm for solving Problem I.

The Simulated Annealing Algorithm was inspired by the annealing process of metals, and involves two key components: an outer loop representing the annealing process and an inner loop based on the Metropolis Algorithm. The outer loop begins

by setting an initial temperature, which decreases proportionally according to a predefined cooling coefficient until a preset termination temperature is reached. This process determines the number of iterations and the overall computational time. The inner loop evaluates changes in the system's internal energy at a given temperature. If the internal energy decreases compared to the previous state, the new state is accepted. However, if the internal energy does not decrease, acceptance is determined probabilistically using probability P . This probabilistic acceptance allows the algorithm to escape local optima, overcoming a key limitation of linear descent methods such as the Newton descent method. The probability P is governed by the Metropolis Criterion, as shown in Eq. (15) (Wu et al., 2018):

$$P = \begin{cases} 1, & E(n+1) < E(n) \\ e^{-\frac{E(n+1)-E(n)}{T}}, & E(n+1) \geq E(n) \end{cases} \quad (15)$$

The simulated annealing algorithm process is illustrated in Fig. 11. In the context of algorithm design, the term "internal energy" corresponds to the pressure loss in each flow channel along a given path. As the temperature decreases during the simulated annealing process, the algorithm randomly generates a set of turning radii for each curved channel while satisfying the design constraints. During this stage, the algorithm ensures that the newly generated curved channels are effectively mutually constrained, avoiding any overlapping configurations.

Subsequently, different combinations of turning radii are compared, and the algorithm iteratively refines these configurations. The iteration process terminates when either the maximum number of iterations is reached, or the pressure loss converges to a stable value. Ultimately, this approach identifies the minimum pressure loss for the channel and determines the optimal turning radius for each curved segment, as shown in Fig. 11.

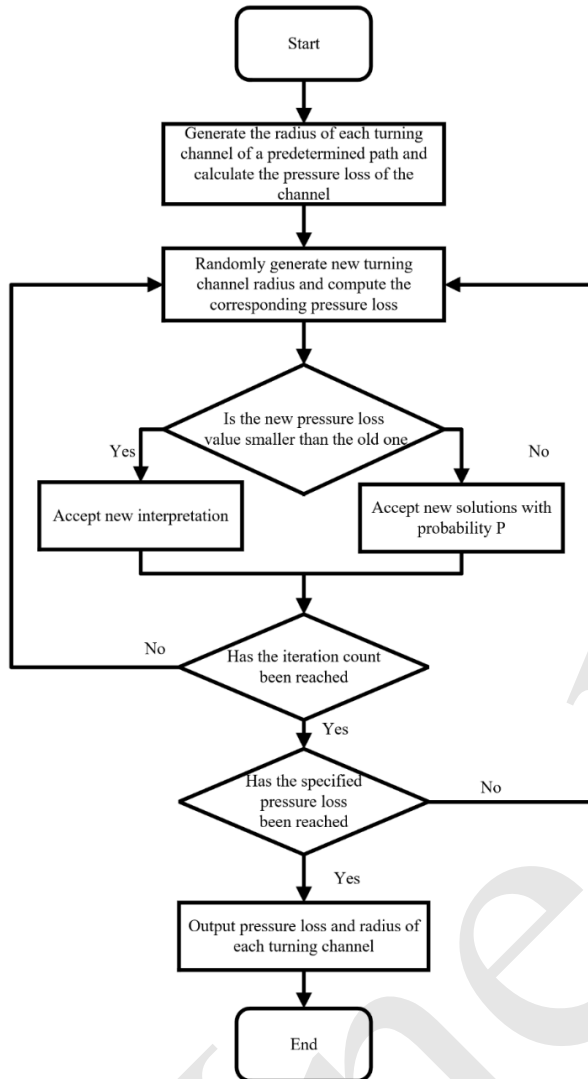


Fig. 11 Simulated annealing algorithm flowchart

The objective of Problem II is to determine the optimal flow path in 3D while satisfying the required design constraints. Achieving this requires evaluating each randomly generated flow path by solving Problem I, wherein the turning radii and pressure losses are calculated. However, this process significantly increases the iteration time due to the need for repeated evaluations. Therefore, selecting an appropriate algorithm for Problem II must consider factors such as the reliability of the algorithm's solutions, whether the error margin is acceptable for engineering standards, and computational efficiency. Considering these factors, the Particle Swarm Optimization (PSO) algorithm, known for its strong global search capabilities and fast convergence, was chosen.

The PSO algorithm is inspired by the collective behavior of bird flocks, where each particle in the swarm represents a potential solution with attributes of velocity and position. Velocity reflects the particle's rate of movement, while position indicates its current direction. Each particle individually searches for the optimal solution within the search space, maintaining a record of its personal best solution, $pbest$. Simultaneously, the algorithm evaluates all particles' solutions to determine the global best solution, $gbest$. Subsequently, each particle adjusts its velocity and position based on both its personal optimal value and the global optimal value. The particle then begins the next iteration to search for the global optimal solution, as shown in Eq. (16) and Eq. (17):

$$V_i = wV_i + C_1 \text{random}(0,1)(pbest_i - X_i) + C_2 \text{random}(0,1)(gbest_i - X_i) \quad (16)$$

$$X_i = X_i + V_i \quad (17)$$

Here, V_i is the velocity of the current particle; X_i is the position of the current particle; w is the inertia factor, which determines the influence of the particle's current state on its subsequent movement; C_1 and C_2 are the acceleration coefficients that control the balance between individual and global learning; $pbest_i$ is the current personal best value for particle i ; $gbest_i$ is the global best value across all particles.

When applying PSO to Problem II, the primary objective is to optimize the positions and angles of turning channels within the flow path. To achieve this, the algorithm focuses on the turning points of the channels. Each particle is defined as a key inflection point in the turning channel, with its velocity and position extended into multiple dimensions to accommodate the 3D nature of the flow path. This multidimensional representation enables the algorithm to explore a wide range of potential configurations, ensuring comprehensive optimization of the flow path.

The velocity and position of particles in the x , y , and z dimensions are updated using Eq. (18) and Eq. (19). However, the concept of an "individual" in our algorithm needs to be more clearly defined; here, an "individual" does not refer to a single particle but rather to a complete flow channel. The individual

optimal solution corresponds to the minimum pressure loss value, $pbest_i$, obtained by solving Problem I when the inflection point coordinates of each turning channel within the current flow channel are determined. At this stage, it is necessary to establish a 1D vector, pB_i , which contains the coordinates of each inflection point of the flow channel. This vector is used when the individual optimum solution is reached to update the iteration speed and spatial position of the inflection points, as shown in Eq. (20):

$$V_i = [V_{ix}, V_{iy}, V_{iz}] \quad (18)$$

$$X_i = [X_{ix}, X_{iy}, X_{iz}] \quad (19)$$

$$pB_i = (P_{i1}, P_{i2}, P_{i3} \dots P_{ij}) \quad (20)$$

Here, i is the i^{th} channel; J is the inflection point of the j^{th} turning channel; P_{ij} is the coordinates of the j^{th} inflection point on the i^{th} channel.

The global optimal solution corresponds to the minimum pressure loss value, $gbest$ across all flow channels. At this stage, it is also necessary to establish a 1D vector, gB , which contains the coordinates of the inflection points for each turning channel when the global optimum is achieved. This vector is used to update the iteration speed and spatial position of the inflection points, as shown in Eq. (21):

$$gB = (G_1, G_2, G_3 \dots G_k) \quad (21)$$

Here, k is the k^{th} inflection point, and G_k represents the coordinates of the k^{th} inflection point on the channel.

Therefore, when updating the speed and position of the inflection points, the coordinates corresponding to both the individual optimal solution and the global optimal solution are updated in the x , y , and z dimensions, as shown in Eq. (22) and Eq. (23):

$$V_{ijx} = wV_{ijx} + C_1 \text{random}(0,1)(P_{ijx} - X_{ijx}) + C_2 \text{random}(0,1)(G_j - X_{ijx}) \quad (22)$$

$$X_{ijx} = X_{ijx} + V_{ijx} \quad (23)$$

Here, the index ijx refers to the x -component (or coordinate) of the j^{th} inflection point of the i^{th} channel.

Therefore, compared to Eq. (16) and Eq. (17), this equation has been expanded to include additional dimensions. Similarly, the same operation is applied to the y and z coordinates of each inflection point, increasing the dimensionality. After each update, it is necessary to determine whether the current global optimal solution, $gbest$, has been reached, or if the algorithm has reached the maximum number of iterations. If neither condition is met, then the update process continues in a loop. If the conditions are met, then the final global optimal solution, $gbest$, and the coordinates, gB , of each inflection point in the channel are output.

The global optimal solution represents the predicted minimum pressure loss value for the flow channel. By connecting the coordinates gB of each inflection point with the inlet and outlet of the flow channel, the flow path is completed. Subsequently, using the turning radius of each turning channel, the input for each turning in the channel is determined, which yields the final channel path and completes the flow channel design. A flowchart of the particle swarm optimization workflow we used is shown in Fig. 12.

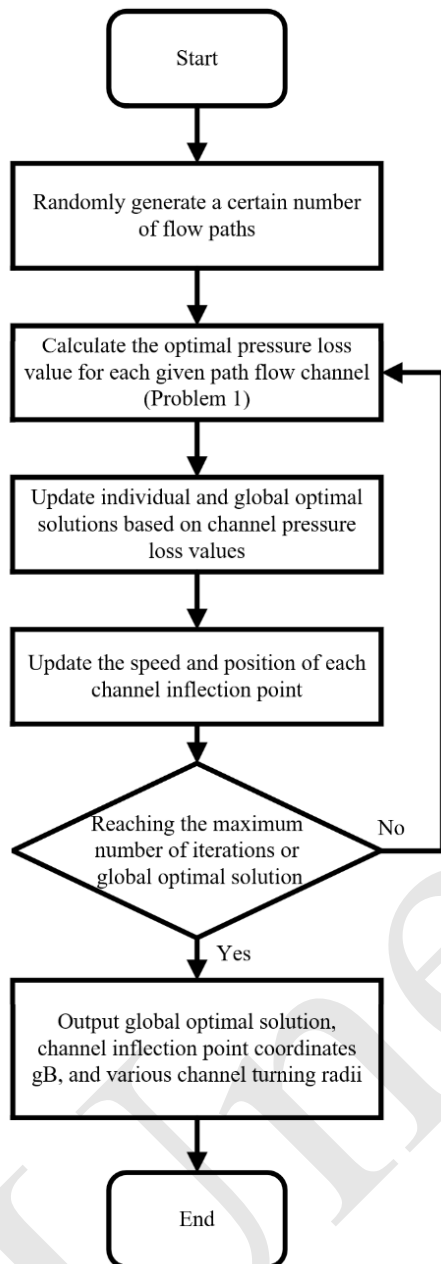


Fig. 12 Particle swarm optimization algorithm flowchart

The overall algorithm for our workflow is illustrated in Fig. 13. This algorithm involves setting the operating conditions of the channel and the entrance/exit locations. It also includes defining the design space of the valve-controlled cylinder based on preliminary design results, establishing the channel's design domain according to constraints, and characterizing and evaluating pressure loss using an objective function for fluid flow in valve-controlled cylinder channels. Additionally, spatial paths for channels are randomly generated using a particle swarm algorithm given the entrance and exit points. This approach utilizes a particle swarm algorithm to randomly generate a series of channels in space for a specific valve-controlled cylinder path, while employing a simulated annealing algorithm to obtain objective function values for each path. Subsequently, optimal solutions for all channels are iteratively solved using the particle swarm algorithm, which reveals the optimal spatial locations and bend designs. Finally, convergence is assessed; if the process converges, the inflection points of various bends along with their radii are output to complete the design of the valve-controlled cylinder channels.

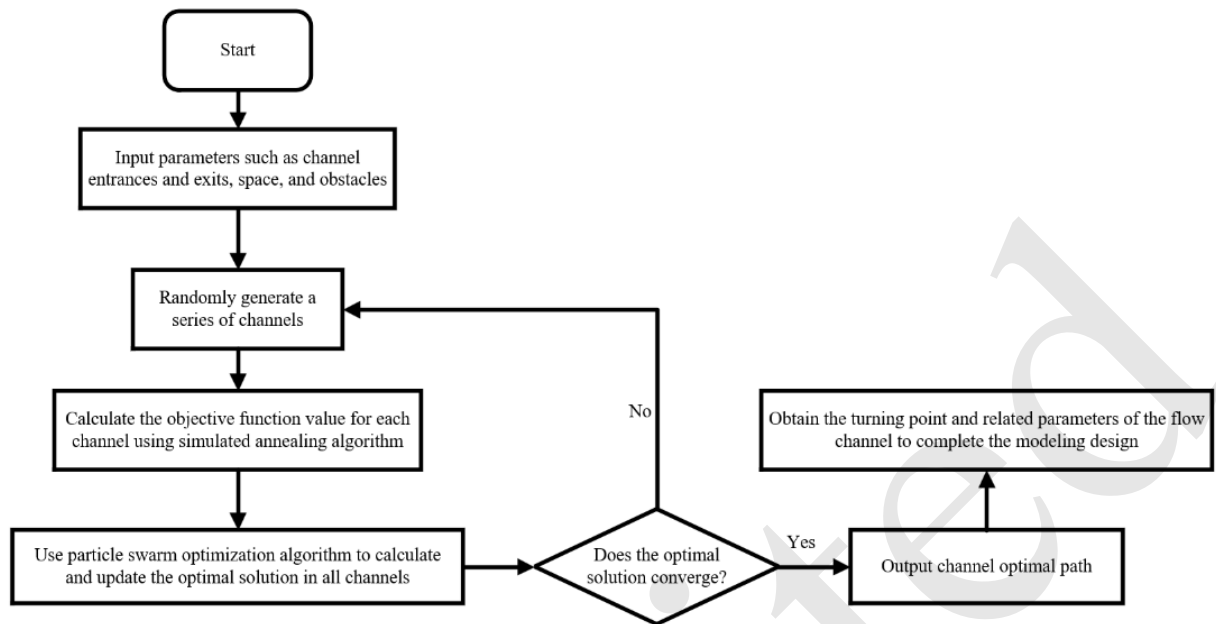


Fig. 13 Automated design solutions for minimizing pressure loss in hydraulic channels

5.4 Design of low-pressure loss flow channels for energy-saving valve-controlled cylinders

The result of applying the above algorithm to design the channel is shown in Fig. 14. The figure demonstrates that the algorithm prioritizes using a large turning radius and angle to minimize pressure loss along the channel while satisfying all constraints (He et al., 2021).

A CFD simulation was performed to validate the

performance of these two flow channels. The simulation parameters are listed in Table 2, with a pressure of 21 MPa and a flow rate of 15 L/min. The measured pressure loss values were 53,883 Pa and 61,457.61 Pa, while the predicted values were 47,142 Pa and 54,921 Pa, resulting in errors of approximately 14.3% and 11.9%, respectively. These results demonstrate the accuracy of the algorithm in predicting pressure loss for both flow channels.

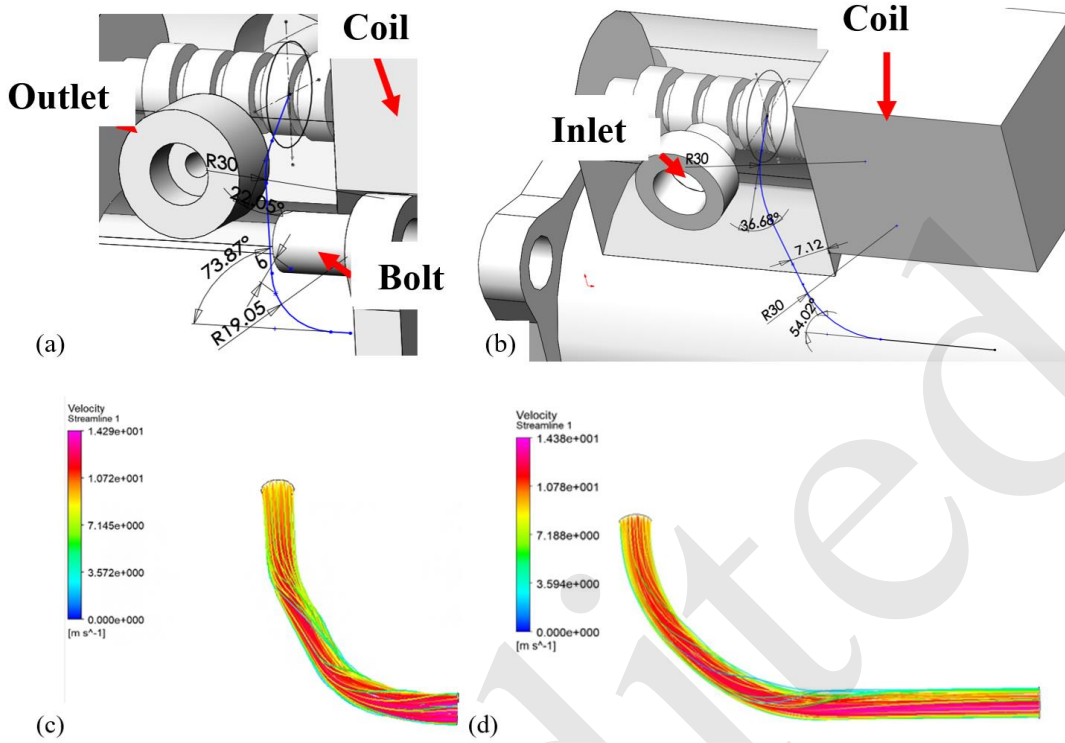


Fig. 14 (a) and (b) Automated design of manifold connections for the integrated valve-controlled cylinder; (c) and (d) Simulation results for the manifold

6 Additive manufacturing and testing of the energy-saving valve-controlled cylinder

Additive manufacturing technology is used for the formation of energy-saving valve-controlled cylinders, with process parameters detailed in Table 3. Given that the traditional prototype is made from 316L stainless steel, 316L stainless steel powder was selected as the forming material based on the operational requirements of the cylinder. Due to the specific characteristics of additive manufacturing, incorporating support structures for certain overhanging features is essential to ensure smooth formation (Jordan et al., 2022; He et al., 2021). The careful addition of these support structures not only improves the quality of the cylinder but also reduces the workload for subsequent machining. As shown in Fig. 15, the spool's position is designed with a 'teardrop' shape to ensure proper formation. Additionally, the barrel on the cylinder body is an overhanging structure and thus requires a shaped channel to facilitate its formation (Zhou et al., 2021).

Table 3 Optimization of process parameters for additive manufacturing of the valve-controlled cylinder

Parameters	Numerical value
Laser power (W)	200
Exposure time (μs)	80
Dot pitch (μm)	60
Scan spacing (μm)	110
Laser point diameter (μm)	70
Scanning strategy	Stripes

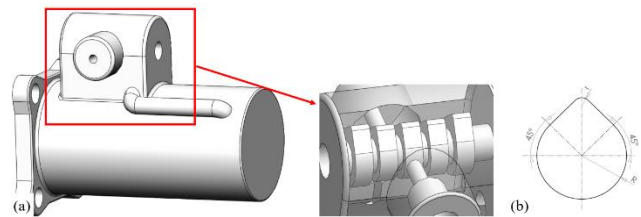


Fig. 15 (a) Structure of the directional valve spool; (b) Support structure with a 'teardrop' shape

After additive manufacturing, the valve-controlled cylinder housing underwent shot peening to improve its surface finish. The cartridge holes and threads necessary for assembly were then machined. Following machining, the end caps, solenoid coils, and piston rods were assembled as shown in Fig. 16. Compared to the traditional prototype

valve-controlled cylinder, the final mass of the integrated cylinder was 7.19 kg, and the maximum space envelope volume was reduced to $201.25 \times 97.12 \times$

135 mm^3 resulting in a weight reduction of approximately 31% and a space volume reduction of about 55%.

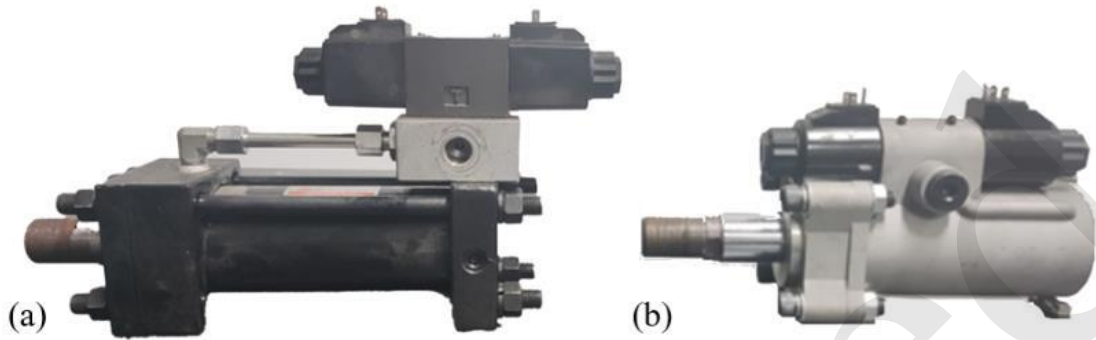


Fig. 16 (a) Prototype of the traditional valve-controlled cylinder; (b) Integrated valve-controlled cylinder

An experimental setup was constructed, as shown in Fig. 17, to measure pressure loss in the flow channel. A turbine flowmeter was used to measure the flow rate in the hydraulic oil pipes, with a range of 3-20 L/min and an accuracy of 1%. Pressure sensors

were employed to detect the oil pressure, with a range of 0-25 MPa and a testing accuracy of 0.075%. A three-phase adapter was used to connect the tested flow channel, pressure sensor, and oil pipe.

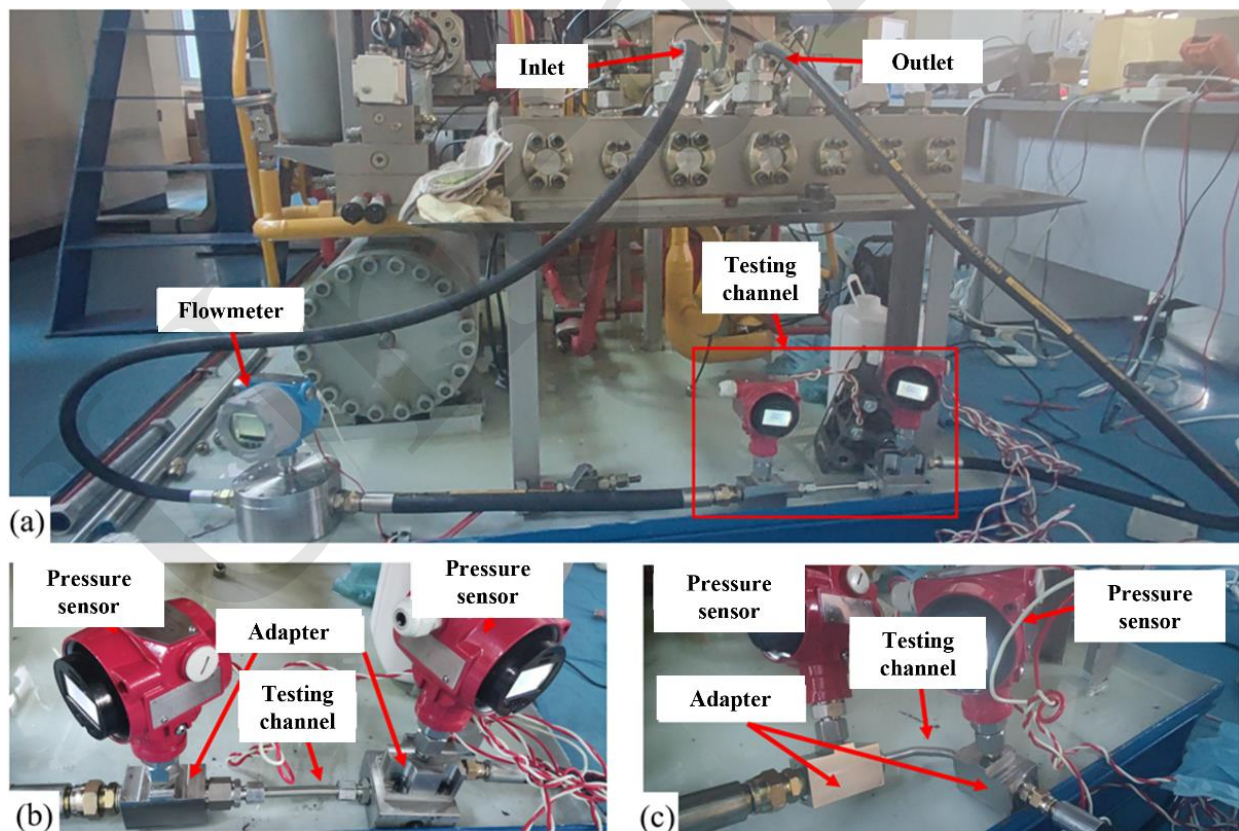


Fig. 17 (a) Experimental design for testing channel pressure loss; (b) Traditional prototype channel testing; (c) Algorithm-generated channel testing

The experimental setup was configured with a pressure of 21 MPa, a working flow rate of 15 L/min, and No. 40 hydraulic oil as the working medium. The hydraulic oil temperature was set to 40 °C. The pressure loss was determined by reading the values from two pressure sensors and subtracting them to obtain the pressure difference. The final pressure loss result was calculated as the average of three test measurements, as shown in Table 4.

Table 4 Pressure loss test results

	Inlet pressure (MPa)	Outlet pressure (MPa)	Pressure loss (MPa)	Average pressure loss (MPa)
Traditional prototype	21	20.9	0.1	0.1
	21.01	20.90	0.11	
	21	20.91	0.09	
Integrated type	21.01	20.95	0.06	0.07
	21.01	20.92	0.09	
	21	20.94	0.06	

The results of the weight, volume, and pressure loss tests are shown in Fig. 18. The integrated valve-controlled cylinder channel significantly reduces pressure loss, showing a 30% improvement over the traditional prototype. However, the algorithm predicts an approximate 16% discrepancy between the simulated and actual experimental values for channel pressure loss, due to factors such as pipe friction not being modeled. Additionally, there is extra pressure loss at the connection point between the channel and the three-phase adapter during the test.

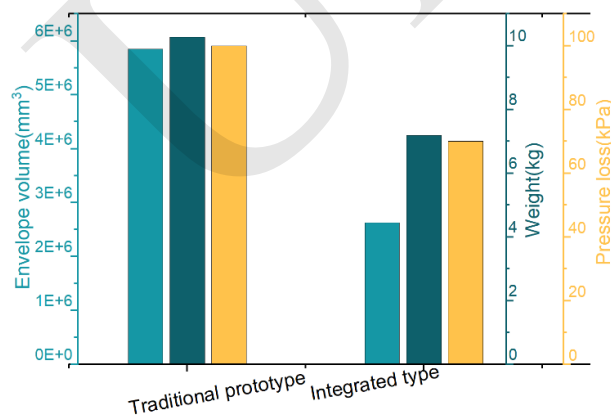


Fig. 18 Comparison of valve-controlled cylinder performance

7 Conclusions

Additive manufacturing processes were used for energy-saving design and integrated molding of valve-controlled cylinders, which were previously machined using conventional methods. Flow performance tests were conducted to evaluate the final integrated valve-controlled cylinder, which was found to have significantly lower weight and volume while also having enhanced flow performance.

We demonstrated that an additive manufacturing approach successfully replicated the traditional prototype's hydraulic principles and allowed for the redesign of valve-controlled cylinder components, eliminating the need for hydraulic valve quick-connects and joints. Moreover, a design guideline for shared wall integration was proposed to minimize the need for print supports and prevent stress concentrations by reducing the distance between the channel and the cylinder. A pressure loss database was also created for channel bends at various operating flow rates, bending angles, and bending ratios. Based on this database, an automated design process for pressure loss-optimized flow channels in valve-controlled cylinders was developed.

Compared to the traditional prototype, the integrated valve-controlled cylinder's weight was reduced by 31%, its volume was 55% lower, and its pressure loss was decreased by over 30%, all while improving flow performance. Based on the results of this study, our proposed design method bolsters the additive manufacturing of valve-controlled cylinders, and may also help with hydraulic valve manifolds and other components with similar structural and connective characteristics.

Acknowledgments

This work was supported by the National Natural Science Foundation of China (Grant No. 52222503), and the Natural Science Foundation of Zhejiang Province (Grant No. LD22E050003).

Compliance with Ethical Standards

Conflict of Interest: On behalf of all authors, the corresponding author states that there is no conflict of interest.

References

Padovani D, Rundo M, Altare G, 2020. The Working Hy-

- draulics of Valve-Controlled Mobile Machines: Classification and Review. *Journal of Dynamic Systems, Measurement, and Control*, 142(7): 070801.
<https://doi.org/10.1115/1.4046334>
- Wu GH, Yang JH, Shang JZ, et al., 2020. A rotary fluid power converter for improving energy efficiency of hydraulic system with variable load. *Energy*, 195: 116957.
<https://doi.org/10.1016/j.energy.2020.116957>
- Zhang JH, Chao Q, Xu B, 2018. Analysis of the cylinder block tilting inertia moment and its effect on the performance of high-speed electro-hydrostatic actuator pumps of aircraft. *Chinese Journal of Aeronautics*, 31(1): 169-177.
<https://doi.org/10.1016/j.cja.2017.02.010>
- Abinab N, Zhang SZ, Tatiana M, et al., 2018. Effect of Zonal Hydraulics on Energy Consumption and Boom Structure of a Micro-Excavator. *Energies*, 11(8):2088.
<https://doi.org/10.3390/en11082088>
- Huang Y, Ming CL, Jyoti M, et al., 2015. Additive Manufacturing: Current State, Future Potential, Gaps and Needs, and Recommendations. *Journal of Manufacturing Science and Engineering*, 137(1): 014001.
<https://doi.org/10.1115/1.4028725>
- S. Pratheesh Kumar, S. Elangovan, R. Mohanraj, et al., 2021. Review on the evolution and technology of State-of-the-Art metal additive manufacturing processes. *Materials Today: Proceedings*, 46(17): 7907-7920.
<https://doi.org/10.1016/j.matpr.2021.02.567>
- K. Satish Prakash, T. Nancharaih, V.V. Subba Rao, 2018. Additive Manufacturing Techniques in Manufacturing -An Overview. *Materials Today: Proceedings*, 5(2): 3873-3882.
<https://doi.org/10.1016/j.matpr.2017.11.642>
- Xie GL, Dong YJ, Sheng ZQ, et al., 2020. Topology optimization design of hydraulic valve blocks for additive manufacturing. *Journal of Mechanical Engineering Science*, 234(10):1899-1912.
<https://doi.org/10.1177/0954406220902166>
- Langelaar M, 2018. Combined optimization of part topology, support structure layout and build orientation for additive manufacturing. *Struct Multidisc Optim*, 57: 1985–2004.
<https://doi.org/10.1007/s00158-017-1877-z>
- Stephen T, David R, Emily C, et al., 2021. Flow in a Simulated Turbine Blade Cooling Channel With Spatially Varying Roughness Caused by Additive Manufacturing Orientation. *Journal of Turbomachinery*, 143(7): 071013.
<https://doi.org/10.1115/1.4050389>
- Zhang C, Wang S, Li J, et al., 2020. Additive manufacturing of products with functional fluid channels: A review. *Additive Manufacturing*, 36: 101490.
<https://doi.org/10.1016/j.addma.2020.101490>
- M. Pietropaoli, R. Ahlfeld, F. Montomoli, et al., 2017. Design for Additive Manufacturing: Internal Channel Optimization. *Journal of Engineering for Gas Turbines and Power*, 139(10): 102101.
<https://doi.org/10.1115/1.4036358>
- Victor B, Octavio A, Dhinesh S, et al., 2018. Highly-Integrated Hydraulic Smart Actuators and Smart Manifolds for High-Bandwidth Force Control. *Frontiers in Robotics and AI*, 5.
<https://doi.org/10.3389/frobt.2018.00051>
- Wang WJ, Tang F, Zheng C, et al., 2021. Prototyping a novel compact 3-DOF hydraulic robotic actuator via metallic additive manufacturing. *Virtual and Physical Prototyping*, 17: 617-630.
<https://doi.org/10.1080/17452759.2022.2045693>
- J. Bhatti, A. R. Plummer, P. Iravani, et al., 2015. A survey of dynamic robot legged locomotion. International Conference on Fluid Power and Mechatronics (FPM), p. 770–775.
 10.1109/FPM.2015.7337218
- Siavash R, Andy A, Ross L, et al., 2018. Robot Leg Design: A Constructive Framework. *IEEE Access*, 6: 54369 - 54387.
 10.1109/ACCESS.2018.2870291
- Huang HP, Zhang JH, Xu B, et al., 2021. Topology optimization design of a lightweight integrated manifold with low pressure loss in a hydraulic quadruped robot actuator. *Mechanical Sciences*, 12: 249–257.
<https://doi.org/10.5194/ms-12-249-2021>
- Tom V, Filippo C, Jérémy B, et al., 2013. Optimization of a U-Bend for Minimal Pressure Loss in Internal Cooling Channels—Part I: Numerical Method. *Journal of Turbomachinery*, 135(5): 051015.
<https://doi.org/10.1115/1.4023030>
- Filippo C, Tom V, Jérémy B, et al., 2013. Optimization of a U-Bend for Minimal Pressure Loss in Internal Cooling Channels—Part II: Experimental Validation. *Journal of Turbomachinery*, 135(5): 051016.
<https://doi.org/10.1115/1.4023031>
- Zhang H, Wang CY, Li CC, et al., 2019. Optimization of Flow Channel in 3D Printing Hydraulic Manifold Block Based on Response Surface Method. IEEE 8th International Conference on Fluid Power and Mechatronics (FPM), p. 217–223.
 10.1109/FPM.2015.7337218
- Shang YX, Liu XC, Jiao ZX, et al., 2018. An integrated load sensing valve-controlled actuator based on power-by-wire for aircraft structural test. *Aerospace Science and Technology*, 77: 117-128.
<https://doi.org/10.1016/j.ast.2018.02.030>
- Quan ZY, Quan L, Zhang JM, 2014. Review of energy efficient direct pump controlled cylinder electro-hydraulic technology. *Renewable and Sustainable Energy Reviews*, 35: 336-346.
<https://doi.org/10.1016/j.rser.2014.04.036>
- Jordan S, Jarred C, Brandon M, 2022. Laser spot size and scaling laws for laser beam additive manufacturing. *Journal of Manufacturing Processes*, 73: 26-39.
<https://doi.org/10.1016/j.jmapro.2021.10.053>
- Michael S, Marion M, David B, et al., 2017. Laser based additive manufacturing in industry and academia. *CIRP Annals*, 66(2): 561-583.
<https://doi.org/10.1016/j.cirp.2017.05.011>
- Xu ZQ, Li WL, Liu XY, et al., 2019. Dynamic characteristics of coupling model of valve-controlled cylinder parallel

- accumulator. *Mechanics & Industry*, 20(3): 306.
<https://doi.org/10.1051/meca/2019006>
- Daniel H, Damiano P, Martin C, 2019. A Comparison Study of a Novel Self-Contained Electro-Hydraulic Cylinder versus a Conventional Valve-Controlled Actuator—Part 1: Motion Control. *Actuators*, 8(4): 79.
<https://doi.org/10.3390/act8040079>
- Zhou L, Zhu Y, Liu HH, et al., 2021. A comprehensive model to predict friction factors of fluid channels fabricated using laser powder bed fusion additive manufacturing. *Additive Manufacturing*, 47: 102212.
<https://doi.org/10.1016/j.addma.2021.102212>
- N. M. Crawford, G Cunningham, S. W. T. Spenc, 2007. An Experimental Investigation into the Pressure Drop for Turbulent Flow 90° Elbow Bends. *Journal of Process Mechanical Engineering*, 221(2):77-88.
<https://doi.org/10.1243/0954408JPME84>
- L. D. Hashan Peiris, Andrew Plummer, Jens Roesner, et al., 2021. Prediction of Flow Path Pressure Drops in Curved Galleries for Additively Manufactured Hydraulic Manifolds. ASME/BATH 2021 Symposium on Fluid Power and Motion Control, V001T01A021.
<https://doi.org/10.1115/FPMC2021-68676>
- Wu XD, Bai WB, Xie Y, et al., 2018. A hybrid algorithm of particle swarm optimization, metropolis criterion and RTS smoother for path planning of UAVs. *Applied Soft Computing*, 73: 735-747.
<https://doi.org/10.1016/j.asoc.2018.09.011>
- He W, Deng QH, Yang GY, et al., 2021. Effects of Turning Angle and Turning Internal Radius on Channel Impingement Cooling for a Novel Internal Cooling Structure. ASME Turbo Expo 2020: Turbomachinery Technical Conference and Exposition, V07AT15A034.
<https://doi.org/10.1115/1.4050608>

Electronic supplementary materials

Section 5, Figs. 4 and 18

中文概要

题目: 一体化阀控缸节能设计与增材制造

作者: 唐洋¹, 李登铤¹, 刘宏毫¹, 张超¹, Wujun WANG², Jie Cai³, 杨华勇¹, 祝毅^{1,4}

机构: ¹浙江大学, 流体动力基础件与机电系统全国重点实验室, 中国杭州, 310027; ²瑞典皇家理工学院能源技术系, 瑞典斯德哥尔摩, 10044; ³中国铁建重工集团股份有限公司, 中国长沙, 410023; ⁴浙江大学宁波科创中心, 中国宁波, 315100

目的: 目前对增材制造成形的阀控缸设计方法研究都停

留在根据既有经验设计元件结构, 均未从科学层面提出增材设计准则及流程。本文旨在提出一种基于增材制造的一体化阀控缸轻量节能设计方法, 通过对某传统加工成形的阀控缸进行了基于增材制造的再设计、再制造, 并对成形的一体化阀控缸进行了性能验证, 来实现轻量节能。

创新点: 1. 提出了管缸贴壁一体化设计准则, 建立了增材制造成形方式下贴壁设计的最小设计间距; 2. 提出了一种低压损流道路径规划方法, 基于模拟退火算法和粒子群算法实现低压损流道路径规划。

方法: 1. 通过仿真和理论分析, 推导出管缸贴壁一体化设计过程中管壁应力变化情况, 比较不同直径比下流道承受的应力(图4), 进而提出增材制造成形方式下贴壁设计的最小设计间距(公式9); 2. 通过仿真分析和插值计算, 得出不同弯曲比、弯曲半径、流速下的流道压损模型(图6), 基于此模型通过模拟退火算法和粒子群算法实现低压损流道路径规划(图11、12、13), 并搭建试验台进行压损测试, 验证所提方法的可行性和有效性(图17、18)。

结论: 1. 基于增材制造技术复现了原型液压原理, 对阀控缸元件进行了重新设计, 去除了液压阀快以及连接接头; 2. 提出了管缸贴壁一体化设计准则, 在避免应力集中情况下缩短流道和缸筒距离, 减少打印支撑; 3. 建立了不同工作流量、弯曲角度和弯曲比下拐弯流道的压损数据库, 并基于此提出了以压损和拐弯数量为导向的阀控缸流道设计流程; 4. 相对于阀控缸原型, 一体化阀控缸的重量减轻了31%, 空间体积减小了55%, 同时主功能流道的压力损失降低了30%以上; 5. 本研究提出一套节能型阀控缸一体化设计流程。同时该设计方法适用于类似结构, 类似连接方式的阀控缸、液压阀块等元件的增材制造设计。

关键词: 阀控缸; 增材制造; 流道路径设计; 节能; 一体化